Journal of Civil Engineering and Construction 2025;14(4):170-187
https://doi.org/10.65720/jcec.2025.14.4.170

Ground Motion Response and Energy Partitioning in 3D Saturated Porous Media: Coupled Effects of Porosity and Poisson's Ratio under P and SV Wave Incidence

Guangrui Feng [1], Liquan Xie [*1], Kaijun Sun[1], Zhaokun Wang[1], Chenwei Luo[1]

1.College of Civil Engineering, Tongji University, Shanghai 200092, China

E-mail address: 2418198894@qq.com; xie_liquan@tongji.edu.cn; KJSun@tongji.edu.cn; 2530756@tongji.edu.cn; 2432385413@qq.com

Received: 1 November 2025; Accepted: 18 December 2025; Available online: 31 December 2025

Abstract: Understanding the dynamic behavior of saturated porous media is critical for seismic hazard assessment and geotechnical engineering, particularly due to the complex interaction between the solid skeleton and pore fluid. This study numerically investigates the seismic wave propagation and subsequent energy partitioning within a three-dimensional saturated porous medium subjected to incident P-wave and SV-wave excitation. A comprehensive parametric analysis is conducted to quantify the isolated and coupled influence of key material properties, namely porosity (ϕ) and Poisson's ratio (v), on the system's dynamic response. The analysis focuses on comparing the resultant reflection coefficients, the full-field displacement components across various directions, and the detailed energy distribution (including reflected, refracted, and dissipated energy) within the ground. The results demonstrate that both porosity and Poisson's ratio exert a significant and complex influence on wave conversion efficiency at the interface. Specifically, variations in these parameters lead to distinct, non-linear changes in surface and subsurface displacement magnitudes and critically control the total seismic energy distribution, dictating the proportion of energy lost through damping and scattering versus that carried by propagating waves. The findings provide essential insights into the poroelastic dynamic characteristics of ground and are vital for the accurate simulation of earthquake-induced ground motions on saturated soil sites.

Key words: Saturated Porous Media; Seismic Wave Propagation; Energy Partitioning; Ground Motion Response; Reflection Coefficient.

1. Introduction

The accurate assessment of seismic hazard and the design of robust geotechnical and structures fundamentally rely on a profound understanding of how seismic waves propagate through and interact with the Earth's subsurface[1][2]. A significant portion of this subsurface, particularly the near-surface soil layers, comprises saturated porous media. In these materials, the dynamic response to seismic excitation is not governed by classical elasticity theory, but by the complex, coupled interaction between the solid skeletal frame and the pore fluid[3]. This necessitates the use of advanced theoretical frameworks to model the ground motion response during an earthquake[4][5].

The standard elastic wave model is inadequate for saturated soils because it fails to account for the relative motion between the fluid and solid phases, a process that is critical for energy dissipation and liquefaction potential[6][7]. To accurately capture these effects, this study utilizes Biot's theory of poroelasticity. Biot's model, a cornerstone of porous media dynamics, elegantly describes the coupled motion, predicting the existence of three distinct types of body waves: two compressional waves, the Fast P1-wave and the Slow P2-wave, and one shear wave, the SV-wave[8][9]. The P1-wave is typically the fastest and involves in-phase motion of the solid and fluid, while the P2-wave is highly diffusive, characterized by out-of-phase motion, and is largely responsible for dissipation mechanisms, including the energy conversion that drives dynamic ground response. Since the dynamic excitation involves both compressional (P) and shear (SV) wave energy, the numerical model is constructed as a 3D interface problem, analyzing the complex scattering and conversion of both incident P-waves and SV-waves at the planar boundary of the saturated porous medium[10][11].

Research into wave propagation at interfaces involving porous media has traditionally focused on analyzing the reflection and transmission coefficients as functions of the incident angle and frequency[12][13][14]. Numerous studies have successfully applied Biot's theory to investigate the reflection phenomena at various boundaries,

including solid-porous, fluid-porous, and porous-porous interfaces[15][16][17]. These analyses have established the strong angular dependence of energy partitioning, often highlighting critical angles where one reflected or refracted wave mode undergoes maximum conversion or entirely disappears. Furthermore, the influence of poroelastic parameters like porosity, permeability, and bulk moduli has been investigated, revealing their direct impact on wave velocities and attenuation[18][19]. For instance, the stiffness and density of the solid frame and the mobility of the pore fluid (controlled by porosity and permeability) are known to strongly modulate the phase velocity and attenuation of the P2-wave[20][21].

However, a comprehensive, systematic, and comparative study that simultaneously investigates the influence of porosity (n) and Poisson's ratio (v) on the full spectrum of seismic response—encompassing kinematic response (displacement and strain components) and the dynamic response (explicit energy partitioning ratios)—remains incomplete, especially within a 3D framework[4][22]. Porosity dictates the fluid content and effective stiffness, while the Poisson's ratio (v), a crucial parameter in the solid skeleton's elastic properties, governs the relative importance of compressional versus shear deformation, thereby directly impacting P-wave and SV-wave velocities and their conversion efficiency[23][24]. A systematic investigation into the coupled effect of these two parameters is essential to move beyond theoretical coefficients and provide practical insights into the magnitude and nature of ground shaking[25][26].

Building upon the established theoretical foundation of Biot's poroelasticity and addressing the identified gap in comprehensive parametric analysis[27][28][29][30], the primary objectives of this study are clearly defined. The findings from this research will provide a new perspective on the roles of material heterogeneity and coupling in seismic dynamics, offering crucial data for refining numerical simulation models and improving the seismic stability criteria used in geotechnical and offshore engineering practices. The remainder of this paper is organized as follows: Section 2 details the theoretical model, presenting Biot's governing equations, the Helmholtz decomposition of the wave fields, and the derivation of the full set of boundary conditions at the fluid-porous interface. Section 3 describes the methodology for solving the resulting matrix system for the unknown wave amplitudes and the subsequent calculation of the energy partitioning ratios. Section 4 presents the comprehensive numerical results, comparing the influence of porosity and Poisson's ratio on reflection coefficients, displacement responses, and energy distribution for both P-wave and SV-wave incidence. Finally, Section 5 synthesizes the key findings, presents the major conclusions, and discusses the implications for geotechnical engineering and seismic hazard assessment.

2. Theoretical model

The theoretical framework for this study, as schematically represented in Fig. 1, is based on the analysis of plane wave reflection and refraction at a planar interface. The model is structurally defined by a a saturated porous elastic medium governed by Biot's poroelastic theory. A Cartesian coordinate system (o−xyz) is established at the interface, with the z-axis directed vertically upwards. The seismic excitation is simulated by a plane wave incident from the bottom of the porous elastic seabed, specifically considering the complex dynamic interactions induced by both P-waves and SV-waves (Shear Vertical wave). The incident energy is partitioned into multiple reflected and refracted waves—including the reflected Fast P-wave (P1), the reflected Slow P-wave (P2), and the reflected Shear Vertical wave (SV)—whose coefficients and energy flux ratios are analyzed as primary indicators of the system's dynamic response. This model setup is crucial for numerically isolating and quantifying the coupled influence of key poroelastic parameters (porosity n and Poisson's ratio v) on the resultant ground motion and energy balance.

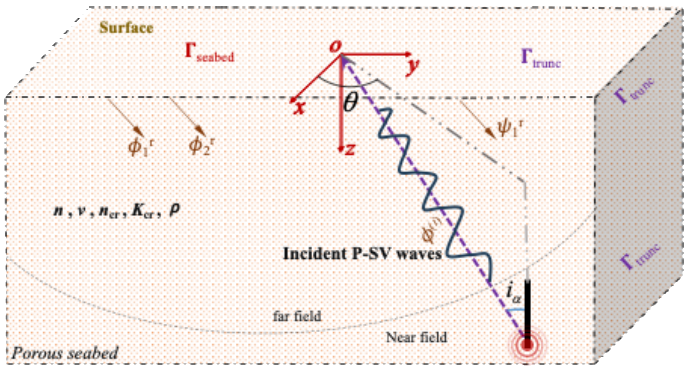

Fig. 1 Geometrical modeling of 3D porous site subjected to the P-SV waves

The dynamic behaviour of the saturated porous seabed is fundamentally governed by Biot's comprehensive theory of poroelasticity, which couples the deformation of the elastic solid skeleton with the diffusive motion of the pore fluid. For a saturated porous medium where the solid frame is assumed to be linearly elastic and isotropic, and the pore fluid is considered to be a compressible, inviscid substance allowing only dilatational deformation, the governing equations of motion (Biot's wave equations) can be elegantly expressed in terms of the solid phase displacement (u) and the fluid flow relative to the solid (U). These equations, derived from the conservation of momentum for both the solid and fluid phases, form the basis for the numerical model and are essential for capturing phenomena such as:

$$\begin{cases} \left(\lambda_{\text{sat}}+2\mu\right)\nabla^2\phi+Q\nabla^2\Phi=\dfrac{\partial^2}{\partial t^2}\left(\rho_{11}\phi+\rho_{12}\Phi\right)+\hat{b}\dfrac{\partial}{\partial t}(\phi-\Phi) \\ Q\nabla^2\phi+R\nabla^2\Phi=\dfrac{\partial^2}{\partial t^2}\left(\rho_{12}\phi+\rho_{22}\Phi\right)-\hat{b}\dfrac{\partial}{\partial t}(\phi-\Phi) \end{cases} \tag{1}$$

$$\begin{cases} \mu\nabla^2\psi=\dfrac{\partial^2}{\partial t^2}\left(\rho_{11}\psi+\rho_{12}\Psi\right)+\hat{b}\dfrac{\partial}{\partial t}(\psi-\Psi) \\ 0=\dfrac{\partial^2}{\partial t^2}\left(\rho_{12}\psi+\rho_{22}\Psi\right)-\hat{b}\dfrac{\partial}{\partial t}(\psi-\Psi) \end{cases} \tag{2}$$

where ϕ,Φ are the P wave potentials for the dry frame and the pore fluid, ψ,Ψ are for the SV wave; $\lambda_{\text{sat}},\mu,Q,R$ are the elastic moduli for a solid-fluid system; $\rho_{11},\rho_{12},\rho_{22},\hat{b}$ are the dynamic mass coefficients and the dissipative coefficient, respectively.

The complex three-dimensional seismic wave field is mathematically described using scalar and vector potential functions, which allow for the decomposition of wave motion into its fundamental components (P-waves and S-waves). The potential function for the incident plane wave (either P-wave or SV-wave) propagating through the saturated porous seabed can be expressed in its generalized three-dimensional form as follows:

$$\phi^{(i)}/\psi^{(i)}\left(x,y,z,t\right)=\exp\left[ik_{1\alpha,\beta}\left(x\sin i_{\alpha,\beta}\cos\theta_{\alpha,\beta}+y\sin i_{\alpha,\beta}\sin\theta_{\alpha,\beta}-z\cos i_{\alpha,\beta}\right)-i\omega t\right] \tag{3}$$

where $k_{1\alpha,\beta}$ are the wave number of the incident waves.

When this incident wave excites the porous medium interface (the porous model), the energy is partitioned into multiple waves to satisfy the boundary conditions. Specifically, the following waves are generated and propagate away from the interface:

$$\phi_1^r\left(x,y,z,t\right)=B_1\exp\left[ik_{1\alpha}\left(x\sin\delta_1\cos\theta_1+y\sin\delta_1\sin\theta_1+z\cos\delta_1\right)-i\omega t\right] \tag{4}$$

$$\phi_2^r\left(x,y,z,t\right)=B_2\exp\left[ik_{2\alpha}\left(x\sin\delta_2\cos\theta_2+y\sin\delta_2\sin\theta_2+z\cos\delta_2\right)-i\omega t\right] \tag{5}$$

$$\psi_3^r\left(x,y,z,t\right)=B_3\exp\left[ik_{\beta}\left(x\sin\delta_3\cos\theta_3+y\sin\delta_3\sin\theta_3+z\cos\delta_3\right)-i\omega t\right] \tag{6}$$

The motion of each of these waves can be expressed in terms of their respective potential functions (Φ1, Φ2, Ψ), where the unknown amplitudes (or coefficients, such as ｜B1｜, ｜B2｜, ｜B3｜) are determined by imposing the continuity of displacement, stress, and fluid pressure at the seabed-seawater interface. where, B_1,B_2,B_3,A_u are unknown coefficients, $k_{\alpha1,\alpha2,\alpha3,\beta,w}$ are wave numbers, and $\delta_{1,2,3w},\theta_{1,2,3,w}$ are reflected angle and rotation angle, respectively.

3. Derivation of wave field

In the context of wave propagation through an isotropic and uniform elastic medium (or the solid skeleton of the porous medium), the complete motion state at any point is determined by the displacement vector $\boldsymbol{u}(\mathbf{r}, t)$. A fundamental principle of wave dynamics allows this complex displacement field to be uniquely decomposed into two independent components, representing the distinct modes of wave travel. The displacement vector $\boldsymbol{u}$ is thus expressed as the sum of two vector fields: the gradient of a scalar potential and the curl of a vector potential, as described by the Helmholtz Decomposition Theorem. These component expressions are subsequently used to

calculate the ground motion response | *Ux* | , | *Uy* | , | *Uz* | and the strain components (e.g., ϵ_{xx}, ϵ_{zz}) presented in the results section, thereby linking the theoretical wave potentials to the observable physical responses of the porous medium.

$$\begin{cases} u_x^s = \dfrac{\partial \phi}{\partial x} + \dfrac{\partial \psi_{3z}}{\partial y} - \dfrac{\partial \psi_{3y}}{\partial z} \\ u_y^s = \dfrac{\partial \phi}{\partial y} + \dfrac{\partial \psi_{3x}}{\partial z} - \dfrac{\partial \psi_{3z}}{\partial x} \\ u_z^s = \dfrac{\partial \phi}{\partial z} + \dfrac{\partial \psi_{3y}}{\partial x} - \dfrac{\partial \psi_{3x}}{\partial y} \end{cases} \qquad \begin{cases} u_x^f = \dfrac{\partial \Phi}{\partial x} + \dfrac{\partial \Psi_{3z}}{\partial y} - \dfrac{\partial \Psi_{3y}}{\partial z} \\ u_y^f = \dfrac{\partial \Phi}{\partial y} + \dfrac{\partial \Psi_{3x}}{\partial z} - \dfrac{\partial \Psi_{3z}}{\partial x} \\ u_z^f = \dfrac{\partial \Phi}{\partial z} + \dfrac{\partial \Psi_{3y}}{\partial x} - \dfrac{\partial \Psi_{3x}}{\partial y} \end{cases} \tag{7}$$

where $u_x^s, u_y^s, u_z^s, u_x^f, u_y^f, u_z^f$ represent solid displacements and fluid displacements at the different directions (x, y, z).

To solve the system of wave equations and determine the unknown amplitudes of the reflected and transmitted waves, the dynamic and kinematic compatibility between the two distinct media must be ensured. This requires that a set of continuous boundary conditions be satisfied exactly at the interface between the upper seawater layer (ideal compressible fluid) and the lower porous elastic seabed (Biot medium).

(1) The zero stress for the solid skeleton

$$\tau_{yz}^s = 0, \qquad \tau_{zx}^s = 0 \tag{8}$$

A defining and crucial feature of Biot's theory of poroelasticity is its prediction of a tripartite wave system propagating through the saturated porous medium, significantly differentiating it from classical elastic theory. Specifically, the dynamic coupling between the solid skeleton and the pore fluid motion gives rise to three distinct bulk wave types whose motion is essential to the analysis of seismic response. Fast Compressional Wave (P1wave) is analogous to the P-wave in an elastic solid, where the solid and fluid phases move in-phase. It is the fastest wave and carries the majority of the seismic energy for compressional motion. Slow Compressional Wave (P2wave) is a unique Biot wave, often highly attenuated, where the solid and fluid phases move out-of-phase (relative motion). It is much slower than the P1 wave and is crucial for energy dissipation and fluid pressure effects within the medium. Shear Vertical Wave (SV wave) is the transverse wave, similar to the S-wave in an elastic solid, and is primarily controlled by the shear modulus of the solid skeleton. The propagation velocities of these three waves are determined by the complex coupling of the elastic properties, fluid bulk modulus, density, and porosity.

$$\begin{cases} \phi = \phi_1 + \phi_2 \\ \Phi = \Phi_1 + \Phi_2 = \eta_1 \phi_1 + \eta_2 \phi_2 \end{cases} \qquad \begin{cases} \psi = \psi_3 \\ \Psi = \Psi_3 = \eta_3 \psi_3 \end{cases} \tag{9}$$

where Φ_1, Φ_2, Ψ_3 are potential functions for fluid phase, and the coefficients η_1, η_2, η_3 can be obtained by following relationship.

$$\eta_j = \frac{A / c_{\alpha,j}^2 - \rho_{11} R + \rho_{12} Q}{\rho_{12} R - \rho_{22} Q} \quad (j = 1, 2), \qquad \eta_3 = -\frac{\rho_{12}}{\rho_{22}} \tag{10}$$

The final step in deriving the analytical solution is to determine the unknown wave amplitudes by formally applying the continuous boundary conditions to the wave potential functions. Specifically, by substituting the potential function expressions (derived in Eqs (4)-(6)) into the set of linear boundary condition equations (Eqs (7) and (8)), we obtain a homogeneous (or non-homogeneous) system of linear algebraic equations. This system couples all the incident, reflected, and transmitted wave amplitudes.

$$\mathrm{AX} = \mathrm{B} \quad \Rightarrow \quad \mathrm{X} = \mathrm{A}^{-1}\mathrm{B} \tag{11}$$

The unknown amplitude coefficients in the vector X are then solved directly by inverting the matrix A, B, as shown in Eq (11). Where, X is unknown coefficients matrix $\mathrm{X} = [B_1, B_2, B_3]^T$. The elements of the matrix A-1 and B are listed to the Appendix 1 when P wave and SV wave incidnet.

Subsequently, the full analytical solution for the dynamic response, including the complete displacement fields and stress/strain components at the seawater-seabed interface, is calculated by substituting these newly determined amplitude coefficients back into the governing potential function expressions (e.g., Eq (7)). This process transforms the theoretical potentials into quantifiable physical results that form the basis of the numerical analysis.

$$\begin{Bmatrix} u_x^s(x,y,z,\omega,t) \\ u_y^s(x,y,z,\omega,t) \\ u_z^s(x,y,z,\omega,t) \end{Bmatrix}_{z=0} = \begin{bmatrix} \dfrac{-i\cdot k_{1\alpha}\cdot\sin i_\alpha\cos\theta_1 / -i\cdot k_{3\beta}\cdot\sin i_\beta\cos\theta_3}{k_{1\alpha}/k_{3\beta}} & \dfrac{i\cdot k_{1\alpha}\cdot\sin\delta_1\cos\theta_1}{k_{1\alpha}/k_{3\beta}} & \dfrac{i\cdot k_{2\alpha}\cdot\sin\delta_2\cos\theta_2}{k_{1\alpha}/k_{3\beta}} \\ \dfrac{-i\cdot k_{1\alpha}\cdot\sin i_\alpha\cos\theta_1 / -i\cdot k_{3\beta}\cdot\sin i_\beta\cos\theta_3}{k_{1\alpha}/k_{3\beta}} & \dfrac{i\cdot k_{1\alpha}\cdot\cos\delta_1\sin\theta_1}{k_{1\alpha}/k_{3\beta}} & \dfrac{i\cdot k_{2\alpha}\cdot\cos\delta_2\sin\theta_2}{k_{1\alpha}/k_{3\beta}} \\ \dfrac{-i\cdot k_{1\alpha}\cdot\sin i_\alpha\cos\theta_1 / -i\cdot k_{3\beta}\cdot\sin i_\beta\cos\theta_3}{k_{1\alpha}/k_{3\beta}} & \dfrac{i\cdot k_{1\alpha}\cdot\cos\delta_1\cos\theta_1}{k_{1\alpha}/k_{3\beta}} & \dfrac{i\cdot k_{2\alpha}\cdot\cos\delta_2\cos\theta_2}{k_{1\alpha}/k_{3\beta}} \end{bmatrix} \quad (12)$$

$$\begin{bmatrix} \dfrac{\pm i\cdot k_{3\beta}\cdot\cos\delta_3\cos\theta_3}{k_{1\alpha}/k_{3\beta}} \\ \dfrac{\pm i\cdot k_{3\beta}\cdot\sin\delta_3\sin\theta_3}{k_{1\alpha}/k_{3\beta}} \\ \dfrac{\pm i\cdot k_{3\beta}\cdot\sin\delta_3\cos\theta_3}{k_{1\alpha}/k_{3\beta}} \end{bmatrix} \cdot \begin{Bmatrix} 1 \\ B_1 \\ B_2 \\ B_3 \end{Bmatrix} \cdot \exp\left[ik_{1\alpha}\left(x\sin i_\alpha / i_\beta\cos\theta_{\alpha/\beta} + y\sin i_\alpha / i_\beta\sin\theta_{\alpha/\beta}\right) - i\omega t\right]$$

where the factor of $\exp\left[ik_{1\alpha}\left(x\sin i_\alpha / i_\beta\cos\theta_{\alpha/\beta} + y\sin i_\alpha / i_\beta\sin\theta_{\alpha/\beta}\right) - i\omega t\right]$ can be factored out from the coefficient matrix in Eq (12) due to the relationship $k_{1x} = k_{2x} = k_{3x} = k_x, k_{1y} = k_{2y} = k_{3y} = k_y$.

A critical aspect of this study is the quantification of how the incident seismic energy is distributed upon interacting with the fluid-porous seabed interface. According to the principle of conservation of energy, the total energy flux carried by the incident wave must be balanced by the sum of the energy fluxes carried by all reflected and transmitted waves.

$$\begin{aligned} E_0 &= \left|\left(v_{11}\cdot\tau_{11} + v_{21}\cdot\tau_{21} + v_{31}\cdot\tau_{31}\right)\right| \quad \Rightarrow \quad \textit{Incident wave} \\ E_1 &= \left|\left(v_{12}\cdot\tau_{12} + v_{22}\cdot\tau_{22} + v_{32}\cdot\tau_{32}\right)\cdot B_1^2\right| \\ E_2 &= \left|\left(v_{13}\cdot\tau_{13} + v_{23}\cdot\tau_{23} + v_{33}\cdot\tau_{33}\right)\cdot B_2^2\right| \quad \Rightarrow \quad \textit{Reflected and Transmitted waves} \\ E_3 &= \left|\left(v_{14}\cdot\tau_{14} + v_{24}\cdot\tau_{24} + v_{34}\cdot\tau_{34}\right)\cdot B_3^2\right| \end{aligned} \quad (13)$$

where E_0, E_1, E_2, E_3 and Eu represent the energy rates for the incident P wave, the reflected P1 wave, the reflected P2 wave, the reflected SV wave, respectively. These energies satisfy the conservation of energy principle $E_0 = E_1 + E_2 + E_3$. And the elements of matrix $\vec{\tau},\vec{v}$ can be obtained from the Appendix 2.

4. Numerical results

This section presents a detailed analysis of the ground motion response and energy distribution within the saturated porous medium, focusing on the sensitivity of the system to variations in the key poroelastic parameters—porosity (n) and Poisson's ratio (v). The primary results are organized into three subsections: the analysis of reflection and conversion coefficients at the interface, the full-field displacement response to incident P and SV waves, and the quantification of energy partitioning (i.e., kinetic, strain, and dissipated energy). All results are derived from the validated finite element model and are presented as a function of the incident angle to highlight the directional dependence of wave phenomena. The following figures illustrate the fundamental relationships between material properties and seismic wave behavior, providing the basis for interpreting the overall dynamic response. Based on the applicability of Biot's theory, the appropriate parameters of seabed and seawater media should be selected for analysis. In this paper, the relevant parameters are $n_{cr} = 0.36$, $K_{cr} = 200$MPa, $K_w = 2190$MPa, $\rho_g = 2095$kg/m^3, $\rho_w = 1000$kg/m^3, p_0=1.18MPa.

Table. 1. Material constants and wave velocities

n	0.15	0.25	0.35
ρ_{11} (kg/m^3)	2336	1946	1661
ρ_{12} (kg/m^3)	-450	-375	-320
ρ_{22} (kg/m^3)	550	625	680
ρ_{dry} (kg/m^3)	1886	1571	1341
ρ_{sat} (kg/m^3)	1986	1821	1701
K_{dry} (MPa)	26,056	11,139	200

v	0.1	0.2	0.3	0.1	0.2	0.3	0.1	0.2	0.3
μ (MPa)	28,424	19,542	12,026	121,52	8354	5141	218.2	150	92.3
α_{dry} (km/s)	5.824	5.257	4.725	4.171	3.765	3.384	0.605	0.546	0.491
β_{dry} (km/s)	3.883	3.219	2.526	2.781	2.306	1.809	0.403	0.335	0.262
α_1 (km/s)	5.756	5.207	4.693	4.174	3.808	3.468	1.833	1.821	1.811
α_2 (km/s)	0.570	0.569	0.567	0.815	0.807	0.796	0.305	0.278	0.251
β (km/s)	3.801	3.152	2.472	2.657	2.203	1.728	0.380	0.315	0.247

(1) P wave incident

The three figures collectively illustrate the distinct impact of varying porosity (n) on the amplitude coefficients (B1, B2, and B3) for a P-wave incident upon a saturated porous interface. The coefficient B1(likely the reflected P-wave) shows a minimum around a 60∘incident angle for all porosities, where the curve for the lowest porosity (n=0.30) dips the deepest, indicating the least P-wave reflection and thus the highest energy partitioning away from the reflected P-wave at that angle. Conversely, the B2 coefficient (likely the P-to-SV converted wave) peaks between 50∘ and 60∘, and its overall magnitude is generally attenuated as porosity increases (from n=0.31to 0.35), suggesting a reduction in wave conversion efficiency with higher pore volume. Finally, the B3 coefficient (potentially representing the transmitted wave or the fluid pressure response) shows significant values greater than 1.0, and its peak magnitude is notably amplified with increasing porosity (with the exception of n=0.30), demonstrating that the increasing volume of the fluid phase in the porous medium significantly enhances this particular wave amplitude or the associated pressure response.

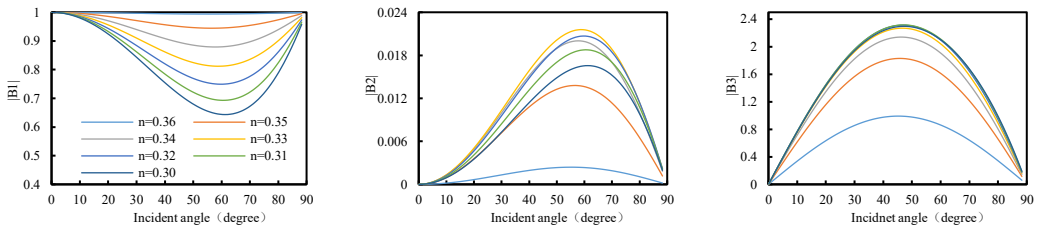

Fig. 3 Amplitude coefficients at the different porosities n.

The analysis of reflection coefficients under a fixed porosity (n=0.36) highlights the critical role of the Poisson's ratio (v) in controlling interface wave dynamics. For B1 (reflected P-wave), decreasing ν leads to a deeper minimum around 55∘, suggesting that a lower Poisson's ratio results in less P-wave energy being reflected and more energy being transmitted across the interface. Conversely, both the B2 (P-to-SV conversion) and B3 (transmitted wave/fluid pressure) coefficients exhibit a clear trend of amplification as the Poisson's ratio decreases. The smallest value of ν=0.1corresponds to the highest peaks for both B2 and B3, indicating that a lower Poisson's ratio significantly promotes P-to-SV wave conversion and enhances the amplitude of the third wave type/pore pressure response. This suggests that media with low Poisson's ratios are more conducive to energy conversion and transmission phenomena at the boundary.

The three displacement plots demonstrate a consistent and significant amplification of ground motion response with increasing porosity (n) across all spatial directions. The horizontal displacement components, $|U_x|$ and $|U_y|$, exhibit typical conversion-driven responses, peaking between 40∘ and 60∘ and converging to zero at normal and grazing incidence. In both cases, the lowest porosity (n =0.30) yields the smallest peak displacement, while the highest porosity (n = 0.36) results in the largest peak displacement (up to ≈2.5for $|U_y|$), indicating that a greater pore volume strongly enhances horizontal shaking. Conversely, the vertical displacement $|U_z|$ starts at its maximum value at normal incidence (0∘), where its magnitude is also directly proportional to the porosity (up to ≈7.0 for n=0.36). Therefore, the results unequivocally establish that increasing the porosity of the saturated medium dramatically increases the total seismic displacement response in both the horizontal and vertical directions under P-wave excitation.

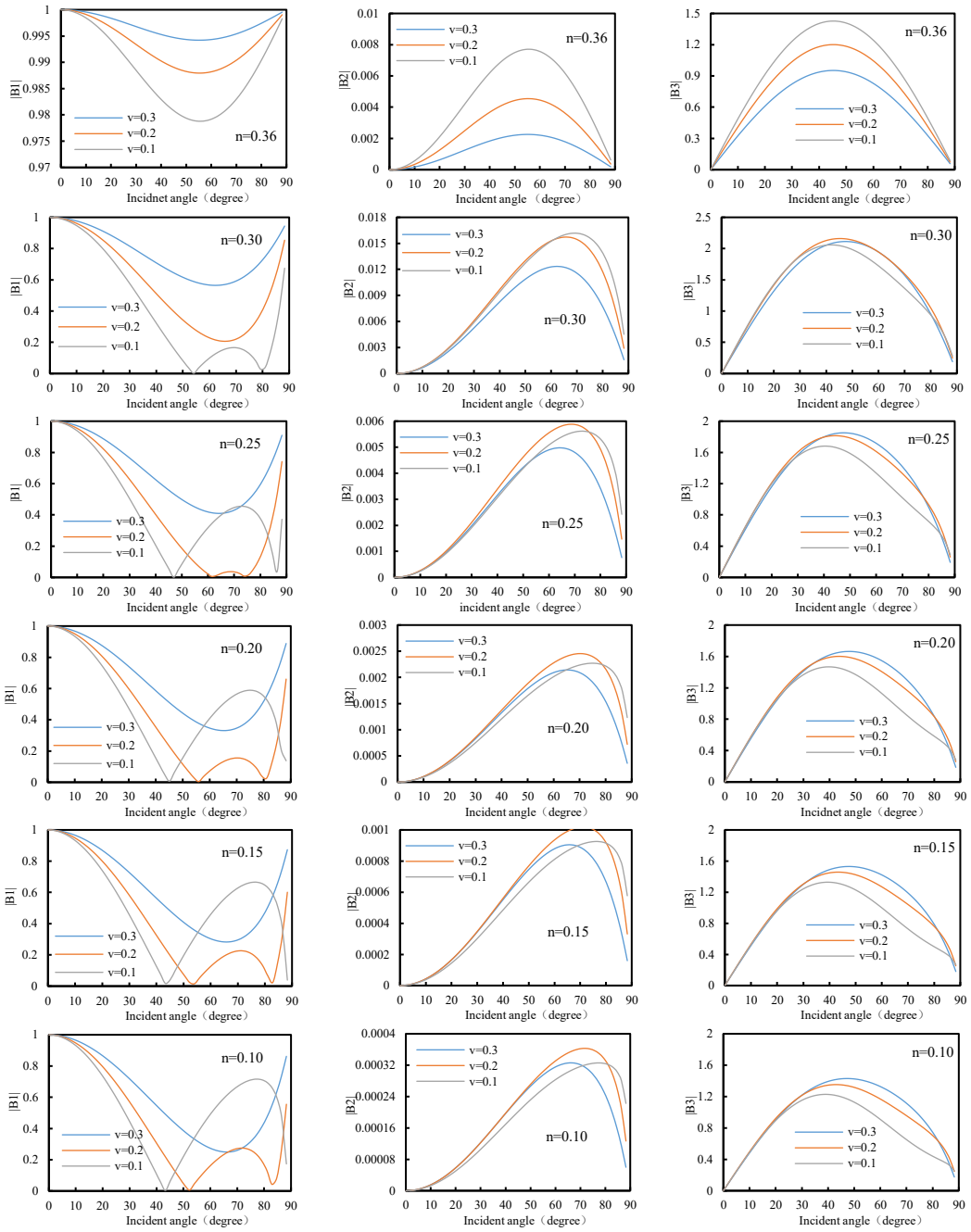

Fig. 4 Amplitude coefficients at the different Poisson ratios *v*.

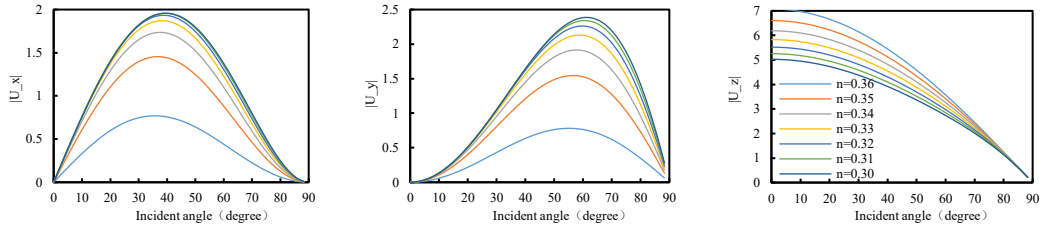

Fig. 5 Displacement amplitude at the different porosities *n*.

The displacement response under varying Poisson's ratios, with a fixed low porosity (n=0.30), reveals a contrasting directional sensitivity. The two horizontal displacement components, $|U_x|$ and $|U_y|$, exhibit maximum amplification when the Poisson's ratio (v) is at its minimum (v=0.1). Specifically, the peak magnitude of $|U_y|$ is significantly larger at v=0.1(≈3.0) compared to v=0.3(≈2.3), confirming that a lower Poisson's ratio enhances horizontal ground motion. Conversely, the vertical displacement $|U_z|$ demonstrates an opposite trend: its magnitude is directly proportional to the Poisson's ratio, with the highest peak at normal incidence observed for v=0.3(≈4.3) and the lowest for v=0.1(≈3.7). This divergent behavior suggests that a lower Poisson's ratio promotes shear-related (horizontal) motion, while a higher Poisson's ratio tends to amplify the P-wave's inherent vertical motion.

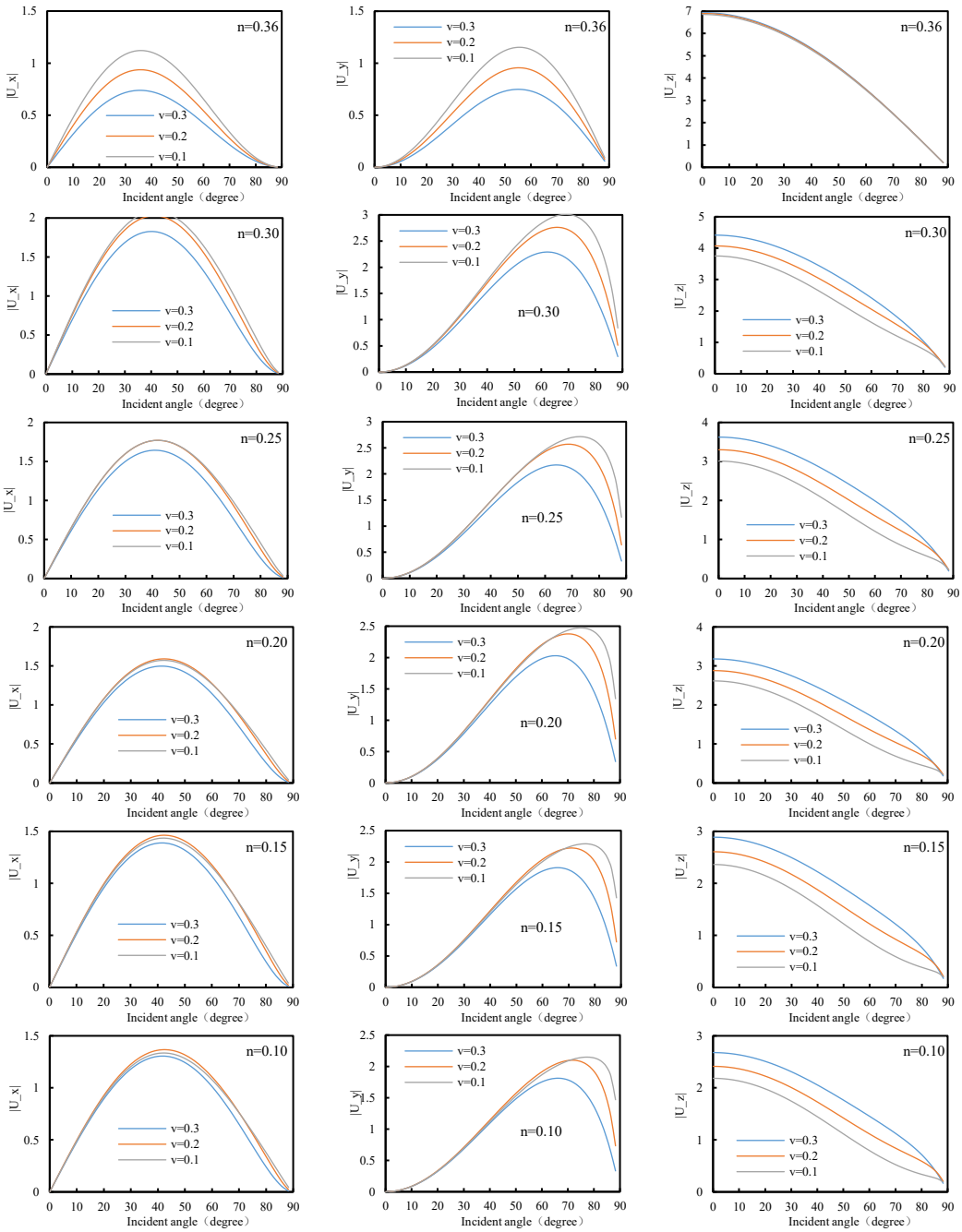

Fig. 6 Displacement amplitude at the different Poisson ratios v.

The analysis of the solid strain components and total displacement under varying porosity (n) with a fixed Poisson's ratio (v=0.30) clearly demonstrates that increasing porosity significantly amplifies both the deformation

and overall ground motion response of the saturated porous medium. The strain components, $|\epsilon_{xx}|$, $|\epsilon_{yy}|$, and $|\epsilon_{zz}|$, all exhibit a similar trend: their peak values are directly proportional to the porosity, with the highest porosity (n=0.34) resulting in peak strains more than double those of the lowest porosity (n=0.15). This robust relationship underscores that a higher pore volume translates into a lower effective stiffness of the medium, enabling larger elastic and shear deformation under the same P-wave energy flux.

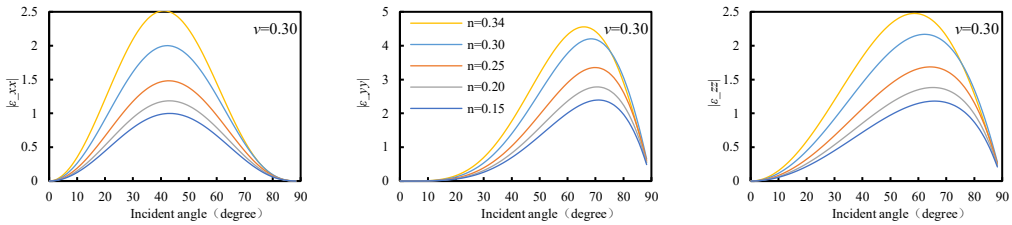

Fig. 7 Strain amplitude at the different porosities n.

Furthermore, the total displacement $|U_{total}|$ shows that the maximum ground motion occurs at normal incidence (0∘) and is drastically increased with rising porosity. Specifically, the maximum $|U_{total}|$ for n=0.34 (≈5.8) is over twice that of n=0.15(≈2.8). This finding, combined with the strain results, provides conclusive evidence that porosity is the dominant parameter controlling the intensity of seismic shaking (displacement) and the extent of material deformation (strain), suggesting a critical role in evaluating seismic vulnerability for highly porous, saturated sites.

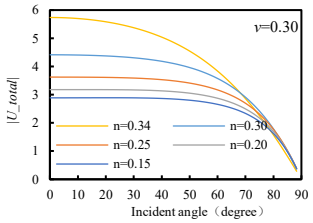

Fig. 8 Total displacement amplitude at the different porosities n.

The four figures illustrating energy partitioning for P-wave incidence, with porosity (n) increasing from 0.25 to 0.34, reveal a key trade-off between the reflected P1 wave (E1) and the converted SV wave (E3). The reflected P1 wave energy (E1) is notably enhanced with increasing porosity, particularly at the critical conversion angles around 60∘, where its minimum value effectively doubles from n=0.25 to n=0.34. This indicates that a higher porosity leads to a stronger reflection of the incident P-wave, reducing the energy available for conversion or transmission. Conversely, the reflected SV wave energy (E3), which dominates the total energy at oblique incidence, is attenuated as porosity increases. The peak E3 value decreases from approximately 0.70 at n=0.25 to 0.60 at n=0.34. In summary, increasing the porosity shifts the energy distribution balance: it diminishes the efficiency of P-to-SV wave conversion (E3) while simultaneously strengthening the direct P-wave reflection (E1) from the saturated porous surface.

The four energy partitioning plots, showing the effect of increasing Poisson's ratio (v) from 0.1 to 0.4 on P-wave incidence, reveal the single most impactful parameter on energy distribution. As Poisson's ratio increases, a massive shift in energy balance occurs, favoring the direct reflection of the P1 wave (E1) over wave conversion (E2 and E3). The minimum energy of E1is dramatically amplified from ≈0.20 at v=0.1to nearly ≈0.90 at v=0.4, indicating that an increasingly higher proportion of incident P-wave energy is reflected back as P1. Concurrently, the energy converted into the reflected SV wave (E3) is severely diminished, with its peak value dropping sharply from ≈0.70 at v=0.1 to almost negligible levels (≈0.08) at v=0.4. The reflected P2 wave energy (E2) also sees a significant reduction. This stark inverse relationship establishes that Poisson's ratio is the primary control on wave-type conversion efficiency: a lower v facilitates significant conversion of P-wave energy into S-wave energy, whereas a higher v confines the energy within the longitudinal P-wave mode.

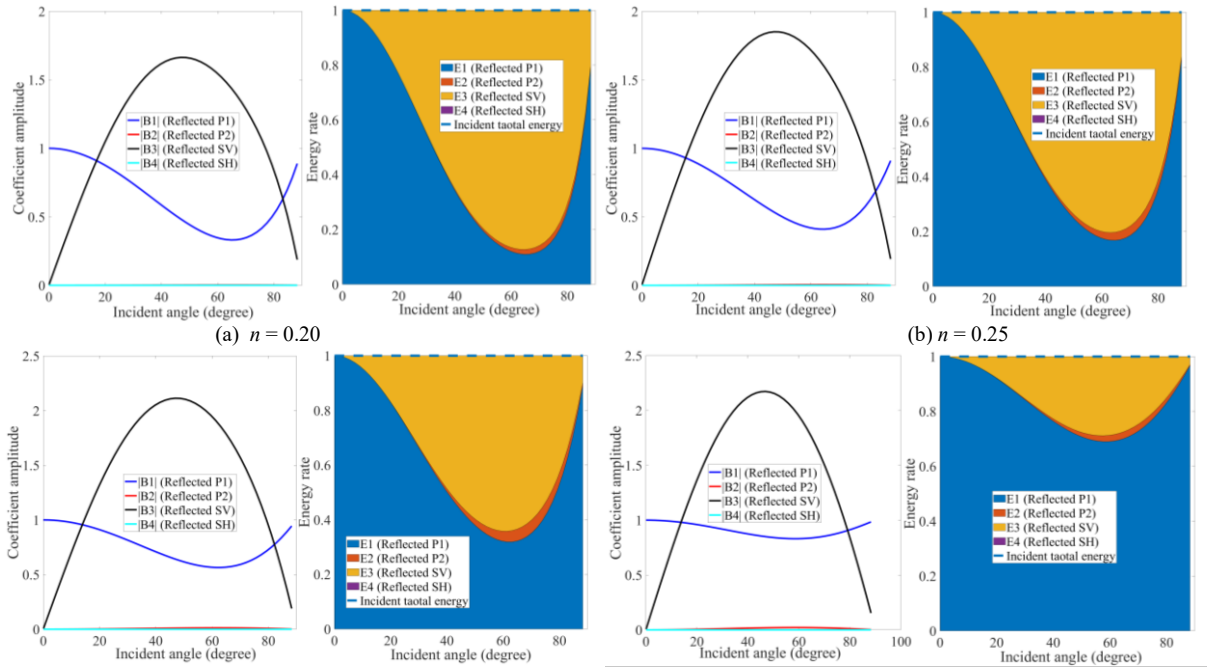

(a) $n = 0.20$ (b) $n = 0.25$

(c) $n = 0.30$ (d) $n = 0.34$

Fig. 9 Energy rates at the different porosity n ($v = 0.30$).

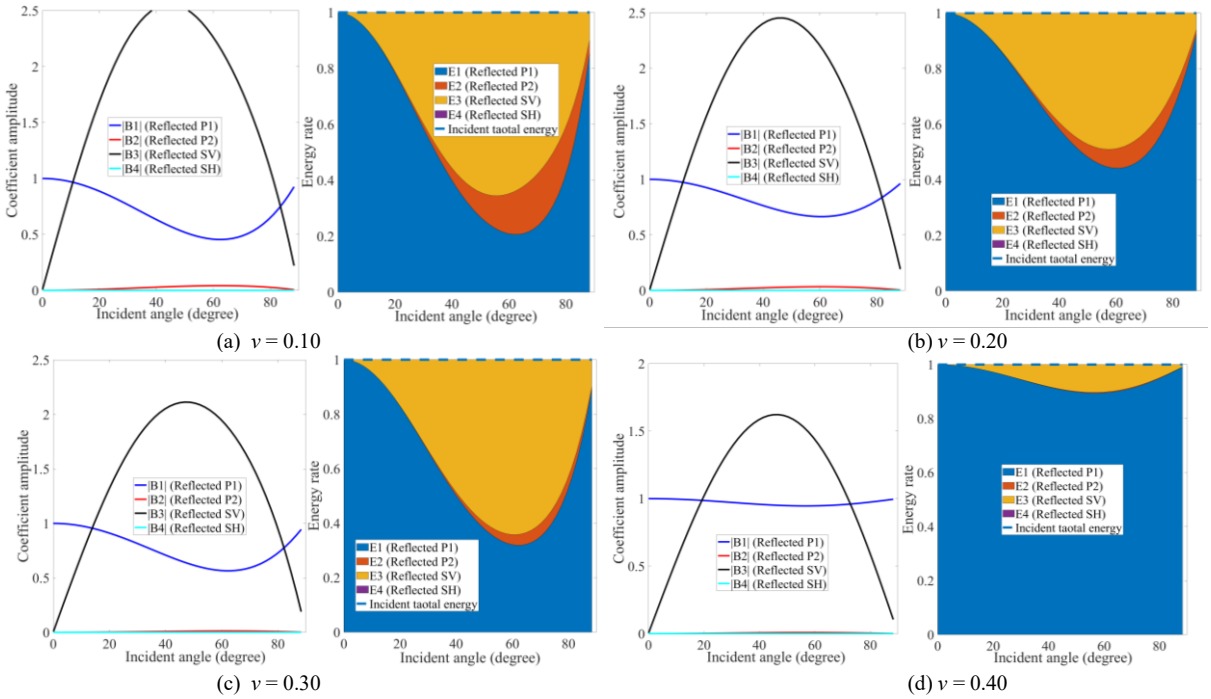

(a) $v = 0.10$ (b) $v = 0.20$

(c) $v = 0.30$ (d) $v = 0.40$

Fig. 10 Energy rates at the different Poisson ratios v ($n = 0.30$).

(2) SV wave incident

The reflection coefficient curves under SV-wave incidence starkly contrast with those observed during P-wave incidence, reflecting fundamentally different energy partitioning mechanisms. The converted P1-wave reflection $|B1|$ exhibits a distinct double-peak profile with a zero-crossing near 45°, unlike the single-valley shape seen in P-wave reflection. Crucially, as porosity (n) increases, the peak amplitudes of $|B1|$ are consistently amplified, indicating that a higher porosity promotes the conversion of SV-wave energy into the

reflected P1-wave. Conversely, the reflected SV-wave coefficient ｜B3｜shows a complex double-trough structure, where increasing porosity leads to deeper troughs (i.e., lower reflection coefficients). This suggests that the increase in porosity, while enhancing the SV-to-P conversion efficiency, simultaneously weakens the direct reflection of the SV-wave, thereby partitioning more energy into the converted P1 and P2 wave modes.

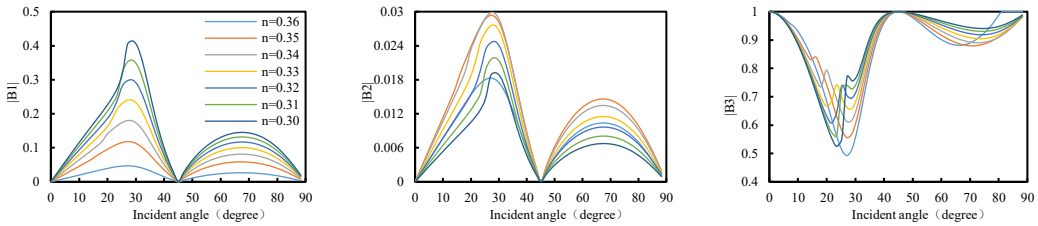

Fig. 11 Amplitude coefficients at the different porosities *n*.

The analysis of reflection coefficients for SV-wave incidence at varying Poisson's ratios (*v*) reveals that Poisson's ratio is the dominant control over the SV-to-P wave conversion efficiency. As the Poisson's ratio decreases, the energy conversion from the incident SV wave to the reflected P1 wave (｜B1｜) is dramatically enhanced, with ｜B1｜reaching its maximum amplitude (approaching 1.0) at *v*=0.1. This conversion efficiency is inversely mirrored by the reflected SV-wave coefficient ｜B3｜, which shows that decreasing *v* leads to a sharp, deeper minimum (approaching zero), indicating that almost all incident SV-wave energy is converted away from the reflected SV mode at specific critical angles. Conversely, the reflected P2-wave coefficient｜B2｜remains very small across all *v* values. In essence, a low Poisson's ratio optimizes the transfer of shear wave energy into longitudinal wave energy at the saturated porous interface.

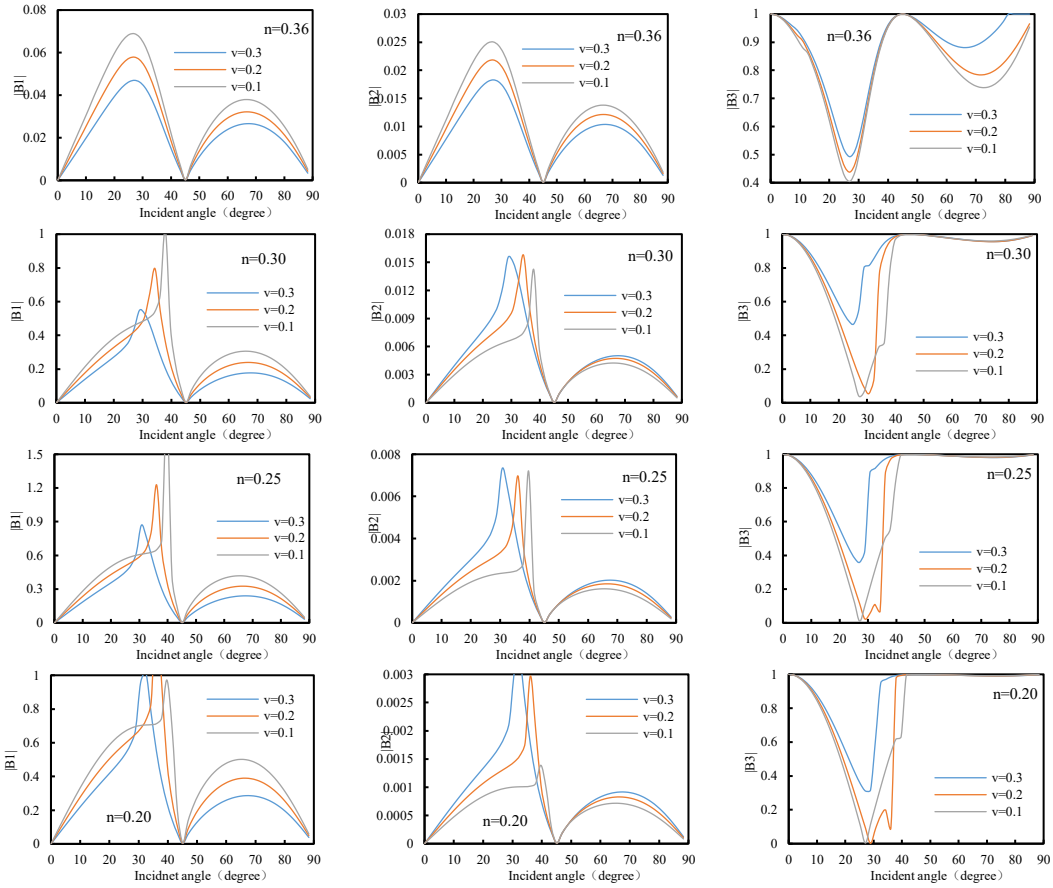

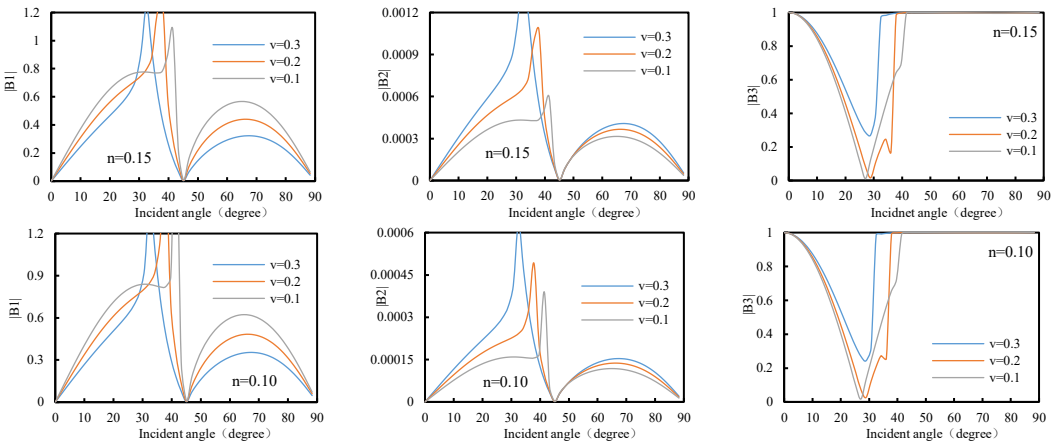

Fig. 12 Amplitude coefficients at the different Poisson ratios *v*.

The analysis of the displacement components under SV-wave incidence across varying porosities (*n*) shows that, similar to P-wave excitation, increasing porosity consistently amplifies the resultant ground motion in all directions. The horizontal component $|U_y|$ exhibits a characteristic double-peak structure with zero displacement at 0∘, where the peak magnitudes are directly proportional to the porosity *n*. Likewise, the vertical component $|U_z|$ follows a single-peak profile (peaking near 40∘) that is also magnified by increasing n. The second horizontal component $|U_x|$ displays a unique and complex response—starting near its maximum at 0∘, featuring a sharp trough near 25∘, and then dropping to zero. Across all its features, the magnitude of $|U_x|$ is also positively correlated with n. This cumulative evidence confirms that porosity acts as a general seismic amplifier in the saturated porous medium, significantly increasing the overall intensity of ground shaking regardless of the incident wave type.

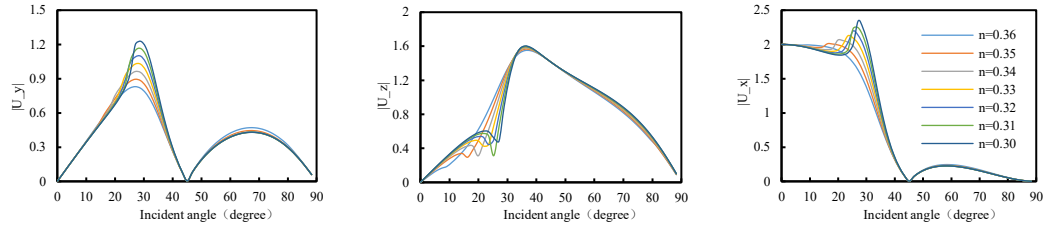

Fig. 13 Displacement amplitude at the different porosities *n*.

The analysis of displacement amplitudes under SV-wave incidence at a fixed low porosity (*n*=0.30) reveals a general but angle-dependent trend: a lower Poisson's ratio (*v*) largely increases the displacement response. Specifically, for the horizontal component $|U_y|$ and the vertical component $|U_z|$, the smallest Poisson's ratio (*v*=0.1) consistently maximizes the peak displacement values, with $|U_y|$ peaking near 1.5 and $|U_z|$ peaking near 1.6. This finding aligns with the energy analysis, where a lower ν facilitates significant wave conversion, leading to greater ground motion. However, the second horizontal component $|U_x|$ displays a more complex behavior: while the lowest ν maintains higher displacement values near 0∘, the highest *v* (*v*=0.3) produces a uniquely high, sharp peak around 30∘. This indicates that the Poisson's ratio strongly controls the angular distribution of displacement, promoting maximum horizontal and vertical shaking at low *v*, but causing highly localized amplification for specific wave components at high *v* angles.

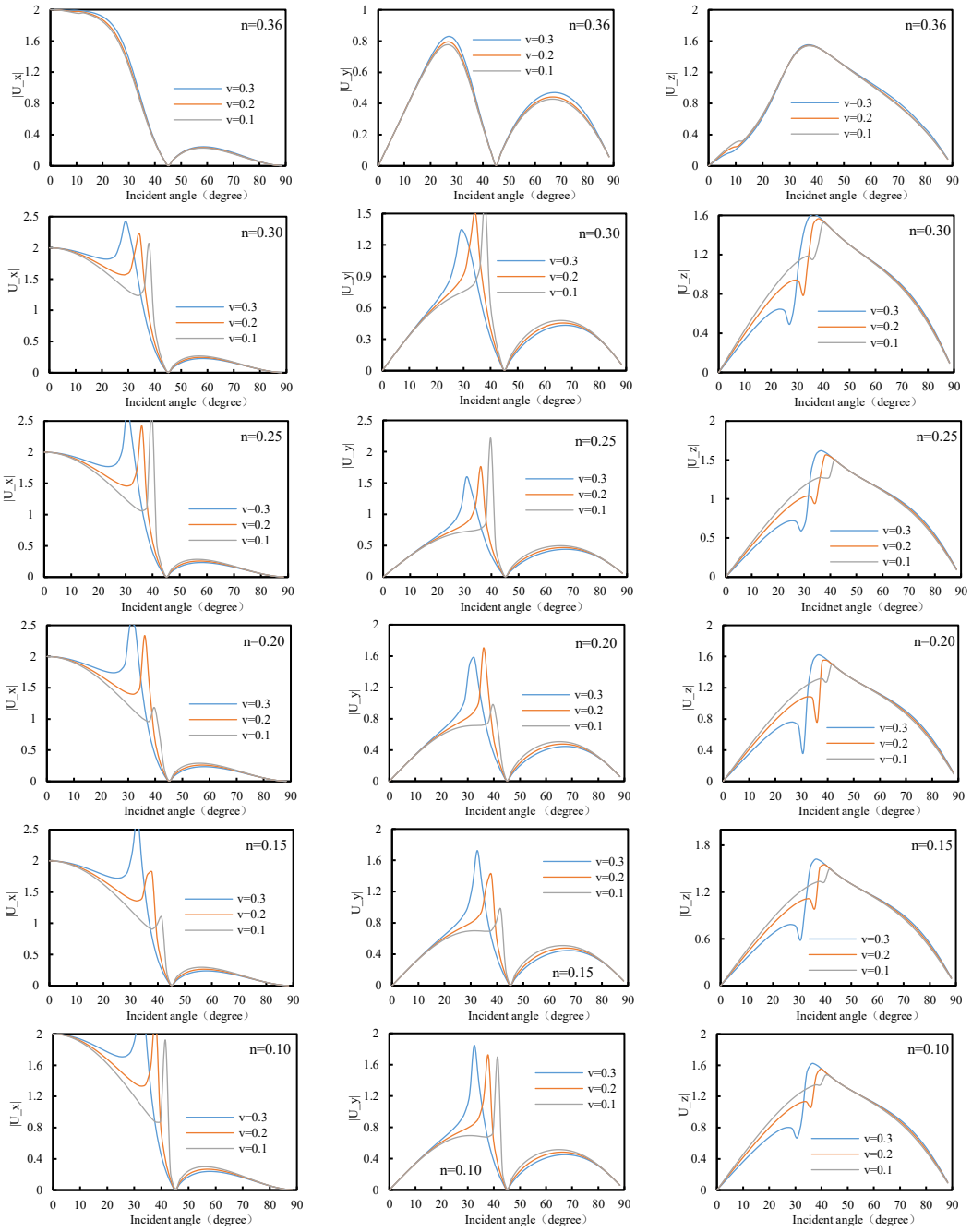

Fig. 14 Displacement amplitude at the different Poisson ratios *v*.

The energy partitioning results for SV-wave incidence confirm the critical role of the SV-P1 critical angle (θ_{crit}), which is demonstrated by a sharp drop in all reflected energy components at $\theta \approx \theta_{crit}$. Notably, as porosity (n) increases from 0.20 to 0.34, the critical angle systematically shifts to smaller incident angles (from 30.9∘ to 21.6∘). This shift implies that higher porosity facilitates the onset of the grazing P1 wave, which is a critical condition for seismic energy transfer. While the total reflected energy plunges to a minimum beyond θcrit (where most energy is transmitted), the change in porosity significantly alters the reflected energy balance at large angles: increasing n dramatically enhances the direct SV-wave reflection (E3) in the oblique-to-grazing range, with its proportion rising from a near-zero level to over 70% of the incident energy. This indicates that at high porosity, beyond the critical conversion region, the SV-wave is predominantly reflected in its original mode.

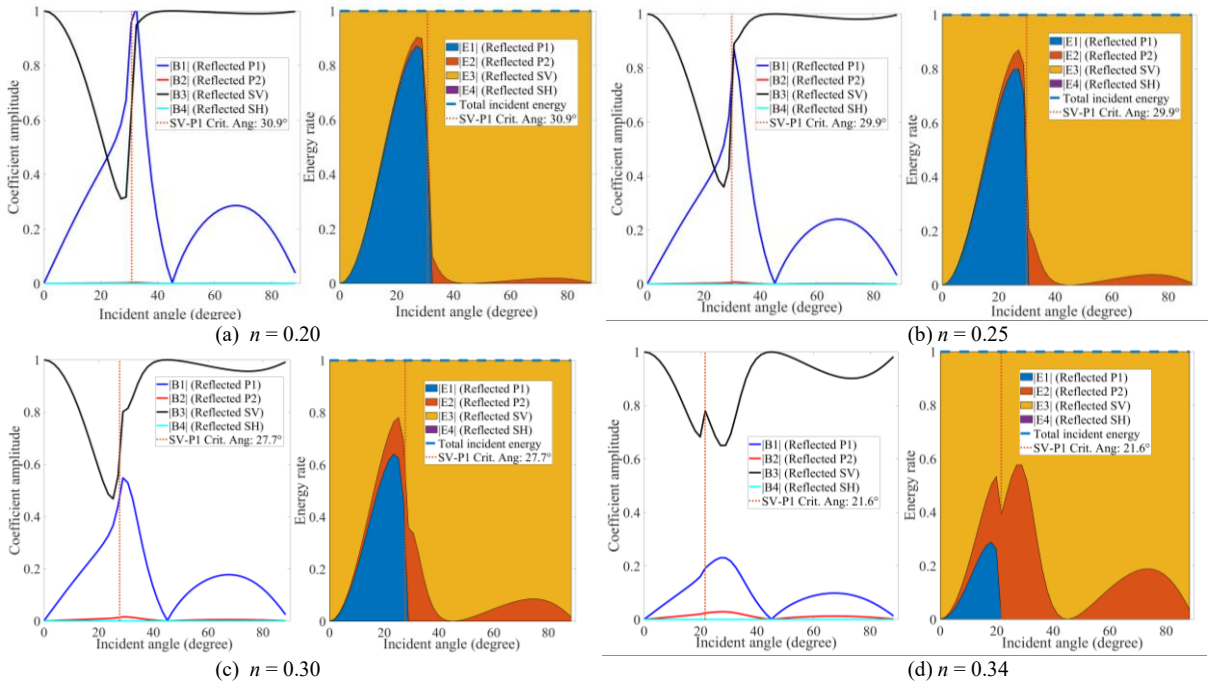

Fig. 15 Energy rates at the different porosity n (v = 0.30).

The analysis of SV-wave energy partitioning under varying Poisson's ratio (v) demonstrates a fundamental restructuring of wave conversion mechanisms as ν increases. The SV-P1 critical angle systematically decreases with increasing ν (from 30.8∘ at v=0.1to15.2∘ at v=0.4), indicating that a higher Poisson's ratio facilitates P1-wave grazing at shallower angles. Crucially, the energy conversion process shifts dramatically: low ν primarily drives the conversion into the fast P1-wave (E1), while high ν drastically suppresses E1 and promotes the conversion into the slow P2-wave (E2). For v=0.4, E2 becomes the dominant converted energy form (≈40% peak), while the reflected SV-wave energy (E3) dominates all other angles (reaching nearly 1.0 between 45∘ and 60∘). This confirms that higher Poisson's ratios inhibit the generation of fast P-waves while favoring the slow P-wave and highly efficient direct SV-wave reflection at the interface.

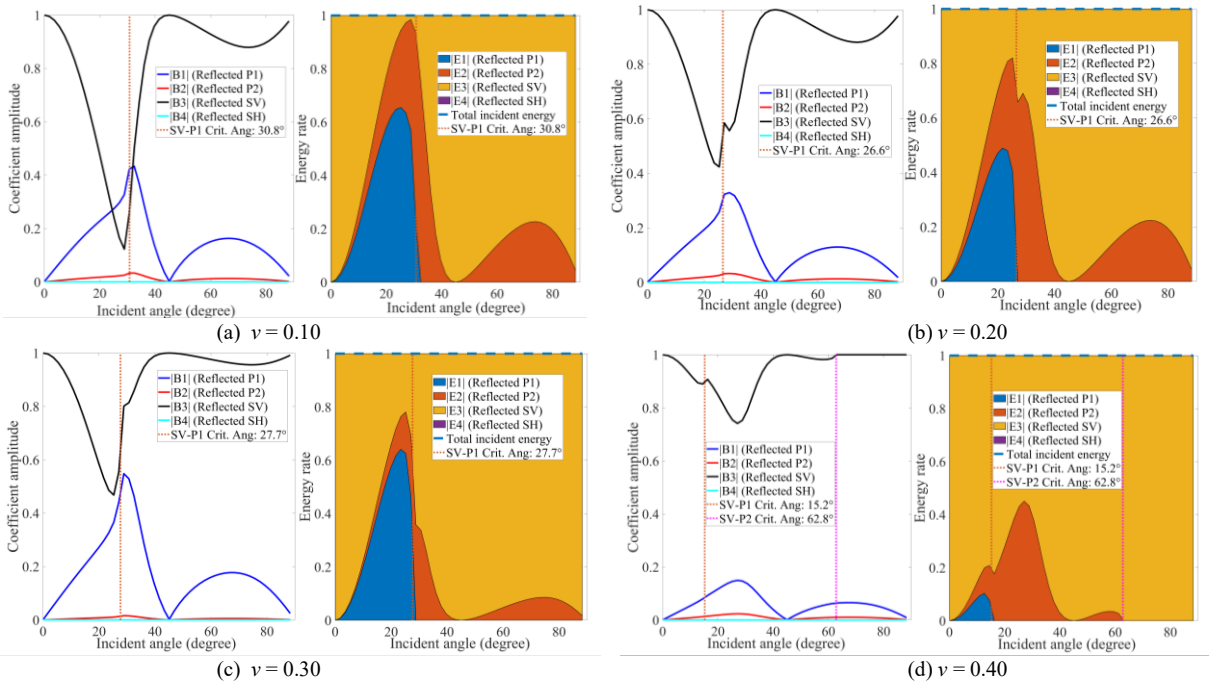

Fig. 16 Energy rates at the different Poisson ratios v (n = 0.30).

5. Conclusions

The comprehensive numerical investigation successfully elucidated the distinct and coupled roles of porosity (n) and Poisson's ratio (ν) in governing the seismic response and energy distribution within saturated porous media. Our findings establish that porosity primarily acts as a ground motion amplifier, increasing both the magnitude of displacement and the degree of material strain across all wave types and incident angles due to the associated reduction in effective stiffness. In stark contrast, the Poisson's ratio serves as a fundamental wave-mode switch, dictating the efficiency and preference of energy conversion at the interface. Specifically, the seismic energy partitioning exhibits a critical trade-off: low ν dramatically promotes conversion into shear and fast P-waves, while high ν inhibits conversion, channeling energy back through direct reflection and, in the SV-case, favoring conversion to the slow P2-wave mode. These results offer vital insights for accurately predicting ground motion and seismic hazard in highly porous, fluid-saturated geological environments.

(1) Porosity (n) acts consistently as the dominant seismic amplifier, irrespective of the incident wave type (P or SV). Increasing n significantly magnifies both the total displacement and strain components in the medium due to the resulting reduction in effective stiffness. The maximum ground motion is observed at normal P-wave incidence for the vertical component (｜Uz｜) and at oblique incidence for horizontal components (｜Ux｜, ｜Uy｜), with all magnitudes being directly proportional to the porosity.

(2) The Poisson's ratio (*v*) fundamentally controls the partition of seismic energy and the efficiency of wave-mode conversion at the interface. A low *v* drastically promotes wave conversion, maximizing the energy transfer from the incident wave to the reflected converted wave (i.e., P-to-SV conversion and SV-to-P1 conversion), which simultaneously leads to a corresponding trough in the energy of the directly reflected wave (｜*E*1｜or ｜*E*3｜).

(3) Increasing the Poisson's ratio (*v*) fundamentally suppresses energy conversion to the fast P1-wave mode while maximizing the direct reflection of the original wave type. Concurrently, increasing both *v* and *n* causes the SV-P1 critical angle (θ_{crit}) to shift to smaller incident angles. For SV-wave incidence, a high *v* triggers a decisive energy switch, effectively diverting the limited converted energy from the fast P1-wave (*E*1) into the slow P2-wave mode (*E*2), while minimizing energy loss through conversion at all other angles.

Appendix 1: The elements of the matrix A^{-1} and B

$$\mathrm{A}^{-1}=\begin{bmatrix}\left(1-\eta_1\right)\cdot k_{1\alpha}\cdot\cos\delta_1\cos\theta_1 & \left(1-\eta_2\right)\cdot k_{2\alpha}\cdot\cos\delta_2\cos\theta_2 & \left(\eta_3-1\right)\cdot k_{3\beta}\cdot\sin\delta_3\cos\theta_3\\ k_{1\alpha}\cdot\cos\delta_1\cos\theta_1 & k_{2\alpha}\cdot\cos\delta_2\cos\theta_2 & -k_{3\beta}\cdot\sin\delta_3\cos\theta_3\\ k_{1\alpha}^2/a_{00}\cdot k_{1\alpha}^2 & a_0\cdot k_{2\alpha}^2/b_{00}\cdot k_{2\alpha}^2 & b_0\cdot k_{3\beta}^2/-k_{3\beta}^2\sin 2\delta_3\cos\theta_3\end{bmatrix}^{-1} \tag{A1-1}$$

$$\mathrm{B}=\begin{bmatrix}\left(1-\eta_1\right)\cdot k_{1\alpha}\cdot\cos i_\alpha\cos\theta_1/\left(1-\eta_3\right)\cdot k_\beta\cdot\sin i_\beta\cos\theta_3\\ k_{1\alpha}\cdot\cos i_\alpha\cos\theta_1/k_\beta\cdot\sin i_\beta\cos\theta_3\\ -k_{1\alpha}^2\cos^2\theta_1/-k_\beta^2\cdot\sin 2i_\beta\cos^2\theta_3\end{bmatrix} \tag{A1-2}$$

where */* left side represent P1 incident and the right side is the SV incident; the coefficients a_0, b_0, a_{00}, b_{00} can be expressed by follows.

$$a_0=\frac{\left[\left(\lambda_{\mathrm{sat}}+\frac{n+1}{n}\cdot Q\right)+\left(Q+\frac{n+1}{n}\cdot R\right)\cdot\eta_2+2G_{sat}\cdot\cos^2\delta_2\sin\theta_2\cos\theta_2\right]}{\left[\left(\lambda_{\mathrm{sat}}+\frac{n+1}{n}\cdot Q\right)+\left(Q+\frac{n+1}{n}\cdot R\right)\cdot\eta_1+2G_{sat}\cdot\cos^2 i_\alpha\cos\theta_1\right]} \tag{A1-3}$$

$$b_0=\frac{\left[-2G_{sat}\cdot\sin\delta_3\cdot\cos\delta_3\cdot\sin\theta_3\cos\theta_3\right]}{\left[\left(\lambda_{\mathrm{sat}}+\frac{n+1}{n}\cdot Q\right)+\left(Q+\frac{n+1}{n}\cdot R\right)\cdot\eta_1+2G_{sat}\cdot\cos^2 i_\alpha\cos\theta_1\right]}$$

$$a_{00}=\frac{\left[\left(\lambda_{\mathrm{sat}}+\frac{n+1}{n}\cdot Q\right)+\eta_1\cdot\left(Q+\frac{n+1}{n}\cdot R\right)+2G_{sat}\cdot\cos^2\delta_1\sin\theta_1\cos\theta_1\right]}{G_{sat}}$$
$$b_{00}=\frac{\left[\left(\lambda_{\mathrm{sat}}+\frac{n+1}{n}\cdot Q\right)+\eta_2\cdot\left(Q+\frac{n+1}{n}\cdot R\right)+2G_{sat}\cdot\cos^2\delta_2\sin\theta_2\cos\theta_2\right]}{G_{sat}} \quad \text{(A1-4)}$$

Appendix 2: The elements of the matrix $\vec{\tau},\vec{v}$

$$\begin{bmatrix} v_{11} & v_{12} & v_{13} & v_{14} \\ v_{21} & v_{22} & v_{23} & v_{24} \\ v_{31} & v_{32} & v_{33} & v_{34} \end{bmatrix}=-\begin{bmatrix} -k_{1\alpha}\cdot\sin i_\alpha\cos\theta_\alpha/k_{3\beta}\cdot\cos i_\beta\cos\theta_\beta & -k_{1\alpha}\cdot\sin\delta_1\cos\theta_1 \\ k_{1\alpha}\cdot\cos i_\alpha\cos\theta_\alpha/k_{3\beta}\cdot\sin i_\beta\cos\theta_\beta & -k_{1\alpha}\cdot\cos\delta_1\cos\theta_1 \\ \eta_1\cdot k_{1\alpha}\cdot\cos i_\alpha\sin\theta_\alpha/\eta_3 k_{3\beta}\cdot\sin i_\beta\cos\theta_\beta & -\eta_1\cdot k_{1\alpha}\cdot\cos\delta_1\sin\theta_1 \end{bmatrix} \quad \text{(A2-1)}$$
$$\begin{bmatrix} -k_{2\alpha}\cdot\sin\delta_2\cos\theta_2 & -k_{3\beta}\cdot\cos\delta_3\cos\theta_3 \\ -\eta_2\cdot k_{2\alpha}\cdot\cos\delta_2\cos\theta_2/k_{3\beta}\cdot\sin\delta_3\cos\theta_3 & k_{3\beta}\cdot\sin\delta_3\cos\theta_3/0 \\ 0/-\eta_2\cdot k_{2\alpha}\cdot\cos\delta_2\sin\theta_2 & \eta_3\cdot k_{3\beta}\cdot\sin\delta_3\sin\theta_3 \end{bmatrix}\cdot\left\{\omega\cdot\exp\left(ik_x x+ik_y y\right)\right\}$$

$$\begin{bmatrix} \tau_{11} & \tau_{12} & \tau_{13} & \tau_{14} \\ \tau_{21} & \tau_{22} & \tau_{23} & \tau_{24} \\ \tau_{31} & \tau_{32} & \tau_{33} & \tau_{34} \end{bmatrix}=\begin{bmatrix} -G_{sat}\cdot\sin 2i_\alpha\cdot k_{1\alpha}^2\cos^2\theta_\alpha/-G_{sat}\cdot\cos 2i_\beta\cdot k_{3\beta}^2\cos^2\theta_\beta & G_{sat}\cdot\sin 2\delta_1\cdot k_{1\alpha}^2\cos^2\theta_1 \\ a_1\cdot k_{1\alpha}^2\cos^2\theta_\alpha/-G_{sat}\cdot\sin 2i_\beta\cdot k_{3\beta}^2\cos^2\theta_\beta/2 & a_1\cdot k_{1\alpha}^2\cos^2\theta_1/a_{01}\cdot k_{1\alpha}^2\cos^2\theta_1 \\ -\left(Q+\eta_1\cdot R\right)\cdot k_{1\alpha}^2\cos^2\theta_\alpha & -\left(Q+\eta_1\cdot R\right)\cdot k_{1\alpha}^2\cos^2\theta_1/-\left(Q+\eta_2\cdot R\right)\cdot k_{2\alpha}^2\cos^2\theta_2 \end{bmatrix} \quad \text{(A2-2)}$$
$$\begin{bmatrix} G_{sat}\cdot\sin 2\delta_2\cdot k_{2\alpha}^2/-G_{sat}\cdot\sin 2\delta_2\cos^2\theta_2 & G_{sat}\cdot\cos 2\delta_3\cdot k_{3\beta}^2\cos^2\theta_3 \\ a_2\cdot k_{2\alpha}^2/a_{02}\cdot k_{2\alpha}^2\cos^2\theta_2 & a_3\cdot k_{3\beta}^2\cos^2\theta_3/G_{sat}\cdot\sin 2\delta_{3\beta}\cdot k_{3\beta}^2\cos^2\theta_3/2 \\ -\left(Q+\eta_2\cdot R\right)\cdot k_{2\alpha}^2\cos^2\theta_2/0 & 0 \end{bmatrix}$$

where */* left side represent P1 incident and the right side is the SV incident; the coefficients a_u,a_{0u},a_1,a_2,a_3 can be expressed by follows.

$$\begin{cases} a_u=\left\{\frac{\left(Q+\eta_1\cdot R\right)\cdot k_{1\alpha}^2}{n}\right\}+B_1\cdot\left\{\frac{\left(Q+\eta_1\cdot R\right)\cdot k_{1\alpha}^2}{n}\right\}+B_2\cdot\left\{\frac{\left(Q+\eta_2\cdot R\right)\cdot k_{2\alpha}^2}{n}\right\} \\ a_{0u}=B_1\cdot\left\{\frac{\left(Q+\eta_1\cdot R\right)}{n}\cdot k_{1\alpha}^2\right\}+B_2\cdot\left\{\frac{\left(Q+\eta_2\cdot R\right)}{n}\cdot k_{2\alpha}^2\right\} \\ a_1=\left[\left(\lambda_{sat}\right)+(Q)\cdot\eta_1+2G_{sat}\cdot\cos^2 i_\alpha\right],\quad a_{01}=-\left[G_{sat}\cdot\cos^2\delta_1+\left(\lambda_{sat}+\eta_1\cdot Q\right)\right] \\ a_2=\left[\left(\lambda_{sat}\right)+(Q)\cdot\eta_2+2G_{sat}\cdot\cos^2\delta_2\right],\quad a_{02}=-\left[G_{sat}\cdot\cos^2\delta_2+\left(\lambda_{sat}+\eta_2\cdot Q\right)\right] \\ a_3=\left[-2\mu\cdot\sin\delta_3\cdot\cos\delta_3\right] \end{cases} \quad \text{(A2-3)}$$

References

[1] Dash HK, Sitharam TG. Effect of frequency of cyclic loading on liquefaction and dynamic properties of saturated sand. International Journal of Geotechnical Engineering 2016;10:487–92. https://doi.org/10.1080/19386362.2016.1171951.

[2] Fu L, Su C, Jin L, Liu X, Li X. Seismic response characteristics of offshore sites in the Sagami Bay, Japan—Part I: Comparison of spectral inversion and ratio under weak motions. Soil Dynamics and Earthquake Engineering 2024;185:108909. https://doi.org/10.1016/j.soildyn.2024.108909.

[3] Liu G, Feng G. Variable seismic motions of P-wave scattering by a layered V-shaped canyon of the second stratification type. Soil Dynamics and Earthquake Engineering 2021;144:106642. https://doi.org/10.1016/j.soildyn.2021.106642.

[4] Lin C-H, Lee VW, Trifunac MD. The reflection of plane waves in a poroelastic half-space saturated with inviscid fluid. Soil Dynamics and Earthquake Engineering 2005;25:205–23. https://doi.org/10.1016/j.soildyn.2004.10.009.

[5] Zhao M, Zhang G, Wang P, Du X, Zhang X. An accurate frequency-domain model for seismic responses of breakwater-seawater-seabed-bedrock system. Ocean Engineering 2020;197:106843. https://doi.org/10.1016/j.oceaneng.2019.106843.

[6] Ta Q-A, Clouteau D, Cottereau R. Modeling of random anisotropic elastic media and impact on wave propagation. European Journal of Computational Mechanics 2010;19:241–53. https://doi.org/10.3166/ejcm.19.241-253.
[7] Goto K, Ishizawa T, Ebina Y, Imamura F, Sato S, Udo K. Ten years after the 2011 Tohoku-oki earthquake and tsunami: Geological and environmental effects and implications for disaster policy changes. Earth-Science Reviews 2021;212:103417. https://doi.org/10.1016/j.earscirev.2020.103417.
[8] Biot MA. Theory of Propagation of Elastic Waves in a Fluid-Saturated Porous Solid. I. Low-Frequency Range. The Journal of the Acoustical Society of America 1956;28:168–78. https://doi.org/10.1121/1.1908239.
[9] Biot MA. Theory of Propagation of Elastic Waves in a Fluid-Saturated Porous Solid. II. Higher Frequency Range. The Journal of the Acoustical Society of America 1956;28:179–91. https://doi.org/10.1121/1.1908241.
[10] Feng G, Xie L. Spatially variable seismic underground motions in layered porous seabed medium induced plane wave. Applied Mathematical Modelling 2024;135:73–89. https://doi.org/10.1016/j.apm.2024.06.036.
[11] Ba Z, Sang Q, Lee VW. 2.5D scattering of obliquely incident seismic waves due to a canyon cut in a multi-layered TI saturated half-space. Soil Dynamics and Earthquake Engineering 2020;129:105957. https://doi.org/10.1016/j.soildyn.2019.105957.
[12] Imtiaz A, Perron V, Hollender F, Bard P, Cornou C, Svay A, et al. Wavefield Characteristics and Spatial Incoherency: A Comparative Study from Argostoli Rock- and Soil-Site Dense Seismic Arrays. Bulletin of the Seismological Society of America 2018;108:2839–53. https://doi.org/10.1785/0120180025.
[13] Li C, Hao H, Li H, Bi K. Theoretical modeling and numerical simulation of seismic motions at seafloor. Soil Dynamics and Earthquake Engineering 2015;77:220–5. https://doi.org/10.1016/j.soildyn.2015.05.016.
[14] Yao Y, Liu T, Zhang J. A new series solution method for two-dimensional elastic wave scattering along a canyon in half-space. Soil Dynamics and Earthquake Engineering 2016;89:128–35. https://doi.org/10.1016/j.soildyn.2016.07.006.
[15] Liu G. Layer-effect on variable seismic ground motions of SV-wave scattered by a double-stratified circular-arc crossing by layer-interface. Soil Dynamics and Earthquake Engineering 2020.
[16] Feng G, Xie L, Chow Su T. SV-wave scattering by an underwater circular cylindrical canyon in a saturated poroelastic half-space. Waves in Random and Complex Media 2023:1–44. https://doi.org/10.1080/17455030.2023.2187240.
[17] Imtiaz A, Perron V, Hollender F, Bard P, Cornou C, Svay A, et al. Wavefield Characteristics and Spatial Incoherency: A Comparative Study from Argostoli Rock- and Soil-Site Dense Seismic Arrays. Bulletin of the Seismological Society of America 2018;108:2839–53. https://doi.org/10.1785/0120180025.
[18] Ba Z, Fu J, Liu Y, Wang Y. Elastic wave field simulation of a three-dimensional sedimentary basin for incident spherical P, SV, and SH waves. Engineering Analysis with Boundary Elements 2021;128:203–15. https://doi.org/10.1016/j.enganabound.2021.04.010.
[19] Jin L, Duan X, Zhou Z, Zhou B, Chen S, Li X. A semi-analytical solution to incident plane P waves scattering by saturated river valley with arbitrary shapes containing water. Soil Dynamics and Earthquake Engineering 2024;179:108566. https://doi.org/10.1016/j.soildyn.2024.108566.
[20] Lu Y, Tan Y, Li X. Stability analyses on slopes of clay-rock mixtures using discrete element method. Engineering Geology 2018;244:116–24. https://doi.org/10.1016/j.enggeo.2018.07.021.
[21] Zhao M, Hu S, Wang P, Zhang C, Zhang G, Du X. Analysis of seawater-sediment-bedrock interaction model under obliquely incident P-SV waves with arbitrary angles. Applied Ocean Research 2023;130:103437. https://doi.org/10.1016/j.apor.2022.103437.
[22] Zhao L, Huang Y, Hu H. Stochastic seismic response of a slope based on large-scale shaking-table tests. Engineering Geology 2020;277:105782. https://doi.org/10.1016/j.enggeo.2020.105782.
[23] Wu M. Seismic response of stratified rock slopes due to incident P and SV waves using a semi-analytical approach. Engineering Geology 2022.
[24] Wu M, Ba Z, Liang J. A procedure for 3D simulation of seismic wave propagation considering source-path-site effects: Theory, verification and application. Earthq Engng Struct Dyn 2022;51:2925–55. https://doi.org/10.1002/eqe.3708.
[25] Guohuan L, Xiao F, Jijian L, Haitao Z, Yi L. Simulation of Spatially Variable Seismic Underground Motions in U-Shaped Canyons. Journal of Earthquake Engineering 2019;23:463–86. https://doi.org/10.1080/13632469.2017.1326427.
[26] Brandow HP, Lee V. Scattering and diffraction of plane P-waves in a 2-D elastic half-space II: shallow arbitrary shaped canyon. Earthq Eng Eng Vib 2017;16:459–85. https://doi.org/10.1007/s11803-017-0395-8.
[27] Chen W-Y, Jeng D-S, Zhao H-Y, Chen G-X, Li X-J. Motion at surface of a gassy ocean sediment layer induced by obliquely incident P waves. Ocean Engineering 2018;149:95–105. https://doi.org/10.1016/j.oceaneng.2017.12.005.

[28] Wu Y, Gao Y, Zhang L, Yang J. How distribution characteristics of a soil property affect probabilistic foundation settlement — from the aspect of the first four statistical moments. Can Geotech J 2020;57:595–607. https://doi.org/10.1139/cgj-2019-0089.
[29] Taslagyan KA, Chan DH, Morgenstern NR. Effect of vibration on the critical state of dry granular soils. Granular Matter 2015;17:687–702. https://doi.org/10.1007/s10035-015-0589-6.
[30] Huang H, Gong W, Khoshnevisan S, Juang CH, Zhang D, Wang L. Simplified procedure for finite element analysis of the longitudinal performance of shield tunnels considering spatial soil variability in longitudinal direction. Computers and Geotechnics 2015;64:132–45. https://doi.org/10.1016/j.compgeo.2014.11.010.